UNIVERSIDADE FEDERAL DO RIO GRANDE DO SUL

FACULDADE DE FARMÁCIA

COHESIVE GEOMETRY OF *Cryptococcus neoformans* DISTRIBUTION MEDIATES FLOWER-LIKE BIOFILM DEVELOPMENT

William Lopes

Orientadora: Profª. Drª. Marilene Henning Vainstein

Porto Alegre

Julho de 2017

William Lopes

COHESIVE GEOMETRY OF *Cryptococcus neoformans* DISTRIBUTION MEDIATES FLOWER-LIKE BIOFILM DEVELOPMENT

Trabalho de Conclusão de Curso apresentado ao Curso de de Farmácia da Universidade Federal do Rio Grande do Sul como pré-requisito para a obtenção do Título de Farmacêutico

William Lopes

Orientadora: Profª. Drª. Marilene Henning Vainstein

Porto Alegre

Julho de 2017

Cohesive Geometry of *Cryptococcus neoformans* Distribution Mediates Flower-Like Biofilm Development

William Lopes[a*], Mendeli H. Vainstein[b*], Glauber R. de S. Araújo[c], Susana Frases[c], Charley C. Staats[a], Rita M. C. de Almeida[b,d], Augusto Schrank[a], Lívia Kmetzsch[a], Marilene H. Vainstein[a]#

Centro de Biotecnologia, Universidade Federal do Rio Grande do Sul, Porto Alegre, Rio Grande do Sul, Brazil[a]; Instituto de Física, Universidade Federal do Rio Grande do Sul, Porto Alegre, Rio Grande do Sul, Brazil[b]; Instituto de Biofísica Carlos Chagas Filho, Universidade Federal do Rio de Janeiro, Rio de Janeiro, Rio de Janeiro, Brazil[c]; Instituto Nacional de Ciência e Tecnologia – Sistemas Complexos, Universidade Federal do Rio Grande do Sul, Porto Alegre, Rio Grande do Sul, Brazil[d].

Running: *C. neoformans flower-like biofilm development*

*These authors contribute equally to this work

#Address correspondence to Marilene H. Vainstein, mhv@cbiot.ufrgs.br

Abstract word count: 208

Text word count: 6624

ABSTRACT

Microbial biofilms are highly structured and dynamic communities, in which phenotypic diversification allows microorganisms to adapt to different environments under distinct conditions. Biofilms are ubiquitous in nature and colonize many niches of the human body and implanted medical devices, being an important factor in *Cryptococcus neoformans* infections. A new approach was used to characterize the underlying geometrical distribution of *C. neoformans* cells during the adhesion stage of biofilm formation. Geometrical aspects of adhered cells were calculated from the Delaunay triangulations and Voronoi diagrams obtained from scanning electron microscopy images (SEM). A correlation between increased biofilm formation and higher ordering of the underlying cell distribution was found. Mature biofilm aggregates were analyzed by applying a novel protocol developed for ultrastructure visualization of cryptococcal cells by SEM. Flower-like clusters consisting of cells embedded in a dense layer of extracellular matrix were observed as well as morphotype switches related to biofilm formation and distinct levels of spatial organization: adhered cells, clusters of cells and community of clusters. The results add insights into yeast motility during the dispersion stage of biofilm formation. This work emphasizes the importance of cellular organization for biofilm growth and may represent novel approaches to establish potential targets for the inhibition and disruption of biofilms with clinical relevance.

IMPORTANCE

The pathogenic yeast *Cryptococcus neoformans* is the major cause of morbidity and mortality due to meningoencephalitis. Biofilm-like structures in medical devices are

related to long-term infections, in general recalcitrant to treatment. In spite of some efforts, essential aspects about the growth mode, properties, ultrastructure and behavior are not well described for fungal biofilms. Our results call to attention an extremely complex and intricate process of biofilm formation where favorable conditions and cellular organization interactively contribute to ultrastructure shaping of biofilms. Combining new approaches using geometrical measures and SEM analysis, we observed that a higher degree of hexagonal order in the distribution of cells during surface adhesion favors biofilm formation. We describe for the first time flower-like clusters of cells embedded in biofilms and distinct levels of spatial organization, possibly regulated in a paracrine manner. These findings may point to new approaches for the development alternative methods for biofilm formation control.

INTRODUCTION

Microorganisms have been traditionally analyzed using planktonic microbial cells; however, this lifestyle is not necessarily related with the growth of microbes in their most prevalent habitat. Recent approaches in confocal microscopy and molecular biology have provided evidence that biofilm formation represents the most common mode of microbial growth in nature (1-4). A wide range of microorganisms is able to switch from a planktonic to a colonial lifestyle in the form of a biofilm, creating aggregated communities that are enclosed by an extracellular matrix (ECM) (2).

Microbial biofilms are now recognized as highly structured and dynamic communities, in which phenotypic diversification allows microorganisms to adapt to

diverse environments under different conditions (5-9). Importantly, biofilms can be composed of thousands of cells encased in a matrix and attached to a surface, but they can also contain as few as tens of cells arranged as small clusters or aggregates (10). Open channels interspersing the microcolonies allow water and nutrients to reach their interior and contribute to the nutrition and formation of mature biofilms, possibly mimicking a primitive circulatory system. Waste products might also be removed through this system (11).

Fungal biofilm formation progresses through three coordinated stages: early, intermediate, and maturation. It begins with the attachment of a microorganism to a surface, followed by a cascade of alterations in gene expression that results in biofilm formation. Specific details of the resulting biofilm depend on surface properties, biofunctionalization, characteristics of the medium, and on the microorganism itself (12-14).

In recent years the role that fungal biofilms play in human disease has received increased attention. Cells growing within biofilms exhibit unique phenotypic features compared to their planktonic counterparts, with the increased resistance to antimicrobial agents provided by biofilms being the more drastic example (3, 15-17).

In this context, biofilm formation by *Cryptococcus neoformans* plays a key role in infection. *C. neoformans* is the etiological agent of cryptococcosis, a lethal disease with a worldwide distribution that affects immunocompromised individuals, resulting in approximately 200,000 deaths per year (18). The major virulence factor of this fungus is the polysaccharide capsule that surrounds the cell wall and is responsible for fungal attachment to surfaces and subsequent biofilm formation (19, 20). The *C. neoformans*

capsule is composed mainly of glucuronoxylomannan (GXM), a polysaccharide generated intracellularly and exported to the extracellular space via vesicle-mediate secretion (21). GXM is also a constituent of the cryptococcal biofilm ECM (22, 23).

*C. neoforma*ns can form biofilms on medical devices, including ventriculoatrial shunt catheters (used to manage intracranial hypertension), peritoneal dialysis fistulae, cardiac valves and prosthetic joints (24-28). On biotic surfaces, after traversing the blood brain barrier in meningoencephalitis, *C. neoformans* has the capacity to form biofilm-like structures known as cryptococcomas (29).

Although previous studies using confocal microscopy provided initial insights into cryptococcal biofilm structure, conventional scanning electron microscopy (SEM) techniques do not preserve the mature biofilm ultrastructure (23, 30). The highly hydrated matrix is greatly deformed and the cell samples undergo distortion and may present artifacts. Also, *C. neoformans* capsule is sensitive to dehydration, easily disrupting during routine sample preparation (31, 32). As a consequence, considerable effort is currently being spent on the development of new methods and instrumentation for its visualization.

We developed and applied a novel modified protocol for SEM that resulted in cryptococcal biofilms samples with better preservation of original structures yielding higher resolution images. With such improved images, we characterized the underlying geometrical structure of cell distribution during biofilm formation. The degree of order was numerically quantified and we revealed a correlation between higher levels of biofilm formation and more ordered underlying structures. Order/disorder are very relevant in physical systems. In crystals, for example, deformations can only occur near defects due to the high energetic cost of their occurrence elsewhere. Besides, some phase transitions

are defect mediated. Moreover, in the last decades the interplay among defects, geometry and statistical physics has been highlighted (33). Here we propose the application of parameters designed to measure order in physical system (34-38) to the microbial populations. We also investigated the details of the ultrastructural organization of cryptococcal biofilms and show that cryptococcal cell aggregates with a specific ordered structure favor biofilm formation as compared to disorganized conglomerates.

RESULTS

Biofilm formation and analysis of cellular adhesion geometry.

To characterize the underlying geometric structure of cell distribution in the initial steps of biofilm formation (after incubation for 4 h), SEM images were examined. This analysis considered the wild type strains *C. neoformans* B3501 and H99, the hypocapsular *grasp* mutant (39) and the acapsular *cap67* mutant (40). To take into account differences in adhesion of the cells to the substrate, we analyzed conditions differing only in the presence or not of poly-L-lysine (PLL). Pre-treatment with PLL increases the number of adhered cells, as expected, but did not influence the cell organization (Fig.1).

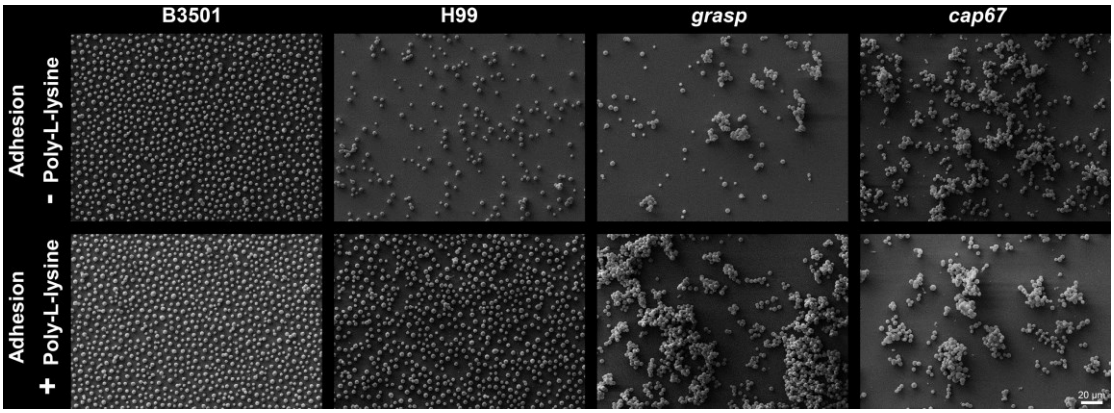

FIG 1 Geometric distribution of cells in the initial steps of biofilm formation, after incubation for 4 h. *C. neoformans* B3501, H99, hypocapsular *grasp* mutant and acapsular *cap67* mutant strains adhered in non-covered glass coverslips (top row) and PLL covered glass coverslips (bottom row).

To classify the spatial distribution of cells, we used four measures: average number of nearest neighbors n and its variance μ_2, intercellular distances, and the average degree of hexagonal order ψ_6. This last measure has been applied to study the liquid-hexatic transition (34, 35) and also to the study of nanoporous alumina arrays in which case the ordering and organization are crucial for engineering applications (38). Among the parameters used, ψ_6 was the one with more conclusive results (Table S1).

The variance of the number of nearest neighbors μ_2 (Eq. 2) was found to be low, in the range 0.7-2.1, indicating that the majority of cells have a number of nearest neighbors very close or equal to the average $n = 6$ (see Fig. S1 for the local values μ_2^i). This fact reinforces that it is adequate to use ψ_6, a measure appropriate for hexagonal symmetry. For its quantification, we first measure the local order parameter ψ_6^i (Eq. 4), that indicates how isotropically arranged the nearest neighbors of the ith cell are. If the cells are found

in a perfect triangular lattice, all sites have six nearest neighbors and the lines joining the i^{th} cell with two of its consecutive neighbors form an angle of $60°$. In this case of perfect hexagonal symmetry, the average of ψ_6^i over the whole sample will attain its maximum value $\psi_6 = 1$. For a random distribution of cells, with angles differing from one another, the local values ψ_6^i will be smaller and their average, ψ_6, will be negative and close to zero (Fig. 10). In the case of partial ordering, one finds intermediate values $0 < \psi_6 < 1$. In Fig. 2A-B, we present the Delaunay triangulation (37), that determines the network of nearest neighbors, combined with SEM of the adhesion stage of biofilm formation without PLL biofunctionalization for B3501 and H99 (wild types). Acapsular *cap67* mutant and hypocapsular *grasp* mutant were not analyzed since they organize in 3D aggregates.

In Fig. 2C, cell color is related to ψ_6^i. It also shows the Voronoi diagram (37), which separates the figure into polygons such that every point in a polygon is closer to the cell inside it than to any other cell. The distribution of ψ_6^i for each image is presented in Fig.2D with a Gaussian fit to the data. The red vertical line represents the average value ψ_6.

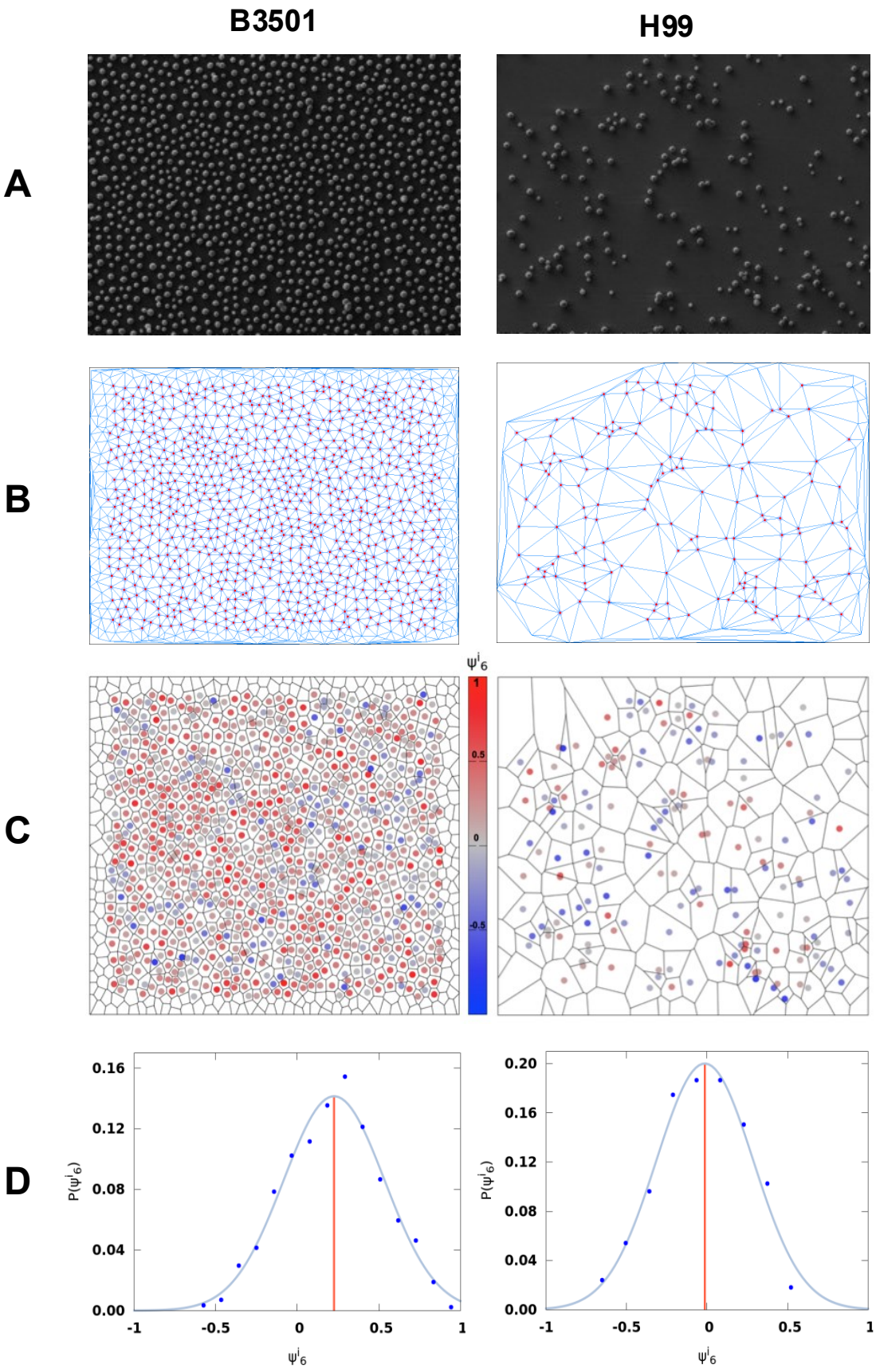
B3501
H99
A
B
C
D
ψ^i_6
1
0.5
0
-0.5
$P(\psi^i_6)$
0.16
0.12
0.08
0.04
0.00
0.20
-1
-0.5
0
0.5
1
ψ^i_6

FIG 2 Analysis of the local order parameter, ψ_6^i, for samples without poly-L-lysine. Left column *C. neoformans* B3501. Right column *C. neoformans* H99. a) SEM image of cryptococcal cells after 4h of adhesion. b) Network of adhered cells; nearest neighbors were obtained by Delaunay triangulation (blue line segments). Red circles represent cell centers in the bulk of the sample. Vertices without circles near the borders represent cells that were discarded from the analysis (distance to the border within 5 % of system size) to minimize border effects. c) Voronoi diagram of the sample. The color code represents ψ_6^i. d) Distribution of ψ_6^i. The blue curve is a Gaussian fit to the data points, grouped into bins. The red vertical line displays the average value ψ_6 of the local order parameter ψ_6^i (Left: $\psi_6 = 0.21$, total number of cells in the image $\mathrm{N_{tot}} = 1064$, number of analyzed cells $\mathrm{N} = 842$, average number of neighbors $n = 6.00$. Right: $\psi_6 = -0.03$, $\mathrm{N_{tot}} = 213, N = 166, n = 5.92$).,

The quantification of biofilm formed after 48 h of incubation was based on 2,3-bis(2-methoxy-4-nitro-5-sulfophenyl)-5-[(phenylamino)carbonyl]-2H-tetrazolium-hydroxide (XTT) reduction assay measurements which determines the absorbance ($A_{(492\ nm)}$) of metabolic activity and correlates with biofilm formation and fungal cell number. We found a correlation ($\mathrm{r}^2 = 0.98$, Fig. 3) between higher levels of biofilm formation ($A_{(492\ nm)}$) and more orderly underlying structures ($\langle\psi_6\rangle$, where the angled brackets represent an average of ψ_6 over 5 images) in the early phase of biofilm formation, since the first layer of cells on a substrate is not necessarily characteristic of a random deposition.

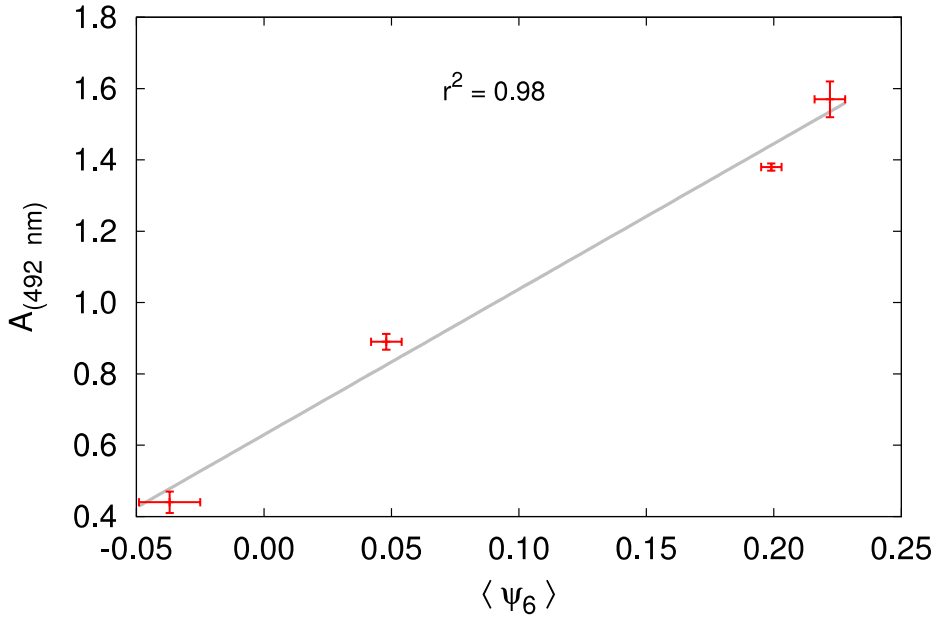

FIG 3 Correlation between biofilm formation measured by the XTT reduction assay (A $_{(492\ nm)}$) and the order parameter $\langle\psi_6\rangle$.

For instance, *C. neoformans* strain B3501, known as a strong biofilm producer has $\langle\psi_6\rangle = 0.20$ and A $_{(492\ nm)}$ = 1.38, while strain H99, a weak biofilm producer, has $\langle\psi_6\rangle = -0.04$ and A $_{(492\ nm)}$ = 0.44 without PLL (Table 1).

Table 1 Average values $\langle\psi_6\rangle$ and A $_{(492\ nm)}$ for different strains and conditions

	***C. neoformans* strains**							
	B3501		***cap67***		**H99**		***grasp***	
	$\langle\psi_6\rangle$	A $_{(492\ nm)}$	$\langle\psi_6\rangle$	A $_{(492\ nm)}$	$\langle\psi_6\rangle$	A $_{(492\ nm)}$	$\langle\psi_6\rangle$	A $_{(492\ nm)}$
Without PLL	0.20	1.38	-	0.17	-0.04	0.44	-	0.20
With PLL	0.22	1.57	-	0.26	0.05	0.89	-	0.42

Special attention should be given to these two strains in the presence of PLL; the better-known biofilm producer B3501 has a significantly more orderly disposal than H99, with an approximately equal number of cells (Fig. 1). These results endorse that the difference in biofilm formation is not due simply to different numbers of cells due to the low adhesion of H99 in the absence of PLL. For both mutants *cap67* and *grasp*, it was not possible to calculate ψ_6 due to the formation of cell agglomerates that result in 3D structures. Nevertheless, this does not weaken the conclusion that a non-random disposal with a regular distance and number of neighbors between cells is important for biofilm formation, given that the cells are closely packed together in these agglomerates.

High values of ψ_6 for *C. neoformans* B3501 in the range 0.18-0.21 (without PLL, Table S1) for the 5 biological replicates analyzed are indeed representative of a non-random distribution since a Student-t test to evaluate the possibility that such values arise from a random deposition of non-overlapping disks with the same average area as the cells yields a p-value $p \approx 3.7 \times 10^{-7}$ (Fig. S2). For the five samples of *C. neoformans* H99, we obtained $p \approx 0.35$ when comparing its ψ_6 values to those of the randomly deposited non-overlapping disks. The same test applied comparing *C. neoformans* B3501 with *C. neoformans* H99 yielded $p \approx 1.1 \times 10^{-6}$. Therefore, it is plausible to conclude that the *C. neoformans* H99 samples present an essentially random distribution, whereas *C. neoformans* B3501 do not (Table 2).

Table 2 Values of ψ_6 for 5 samples of each of the strains B3501 and H99 (without PLL).

	ψ_6 values of *C. neoformans* strains	
Biological replicate	**B3501**	**H99**
1	0.213	-0.058
2	0.200	-0.029
3	0.200	-0.058
4	0.185	-0.039
5	0.199	0.006

The orderly distribution of cells even during the detachment stage of biofilm is a process that occurs dynamically (see Movie S1). From the snapshots, it can be seen that new cells that flow into the already populated region do so by following almost the same paths and tend to maintain a more or less regular distance from other cells. This suggests that the ordering stems from physical, rather than biological processes; for the case at hand one is reminded of like charged spheres, which tend to auto-organize due to the electrical repulsion among them. The cells with their charged capsules due to GXM can be, in a first approximation, regarded as spheres with similar charges (Fig. 4). This is further corroborated by the fact that both mutants with capsular defects tend to agglomerate into compact clusters of cells.

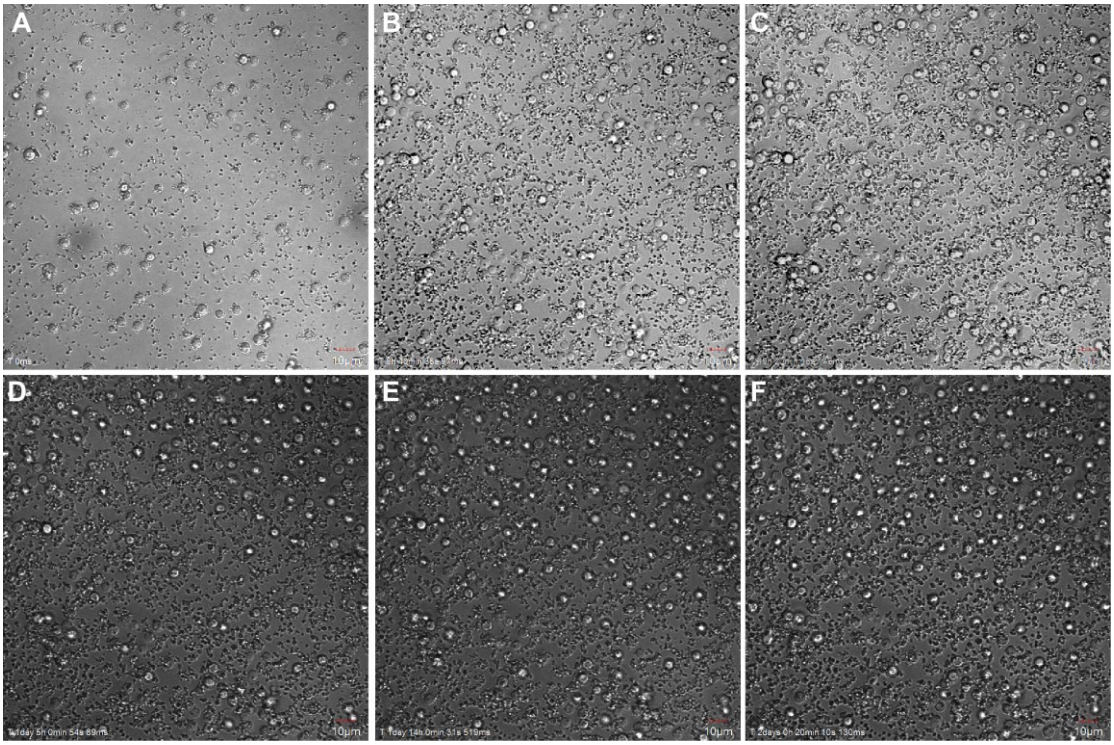

FIG 4 Time-lapse microscopy of *C. neoformans* B3501 flow during various stages of biofilm formation. Initial steps of biofilm formation (A-C). From 24 h onwards, cells enter the vision field from the top (D) and auto-organize (E-F). Cells tend to follow similar trajectories. Snapshots from the Movie S1.

C. neoformans biofilms are organized in flower-like clusters.

We believe that the organized geometrical structure is an important factor for the next steps of biofilm formation. The strain B3501 was used for ultrastructure analysis of biofilm due to its significantly more orderly disposal during adhesion stage (Fig. 2) and strong biofilm formation (30). The applied protocol allowed the detailed observation of preserved cryptococcal biofilms by SEM. Our findings contrast with available data of confocal and optical microscopy in which resolution and detail are limited, but converge in biofilm thickness in the range of 50-76 μm, as well its complexity (15, 30, 41, 42). The

images showed the ECM embedding cells organized into biofilm clusters with both amorphous and organized flower-like structures of the mature biofilm (Fig. 5A-D). The vertical growth seems to dominate cluster expansion with regions of high ECM densities. Isolated yeast cells were found both attached to the surface and cluster-associated (Fig. 5A, C-D).

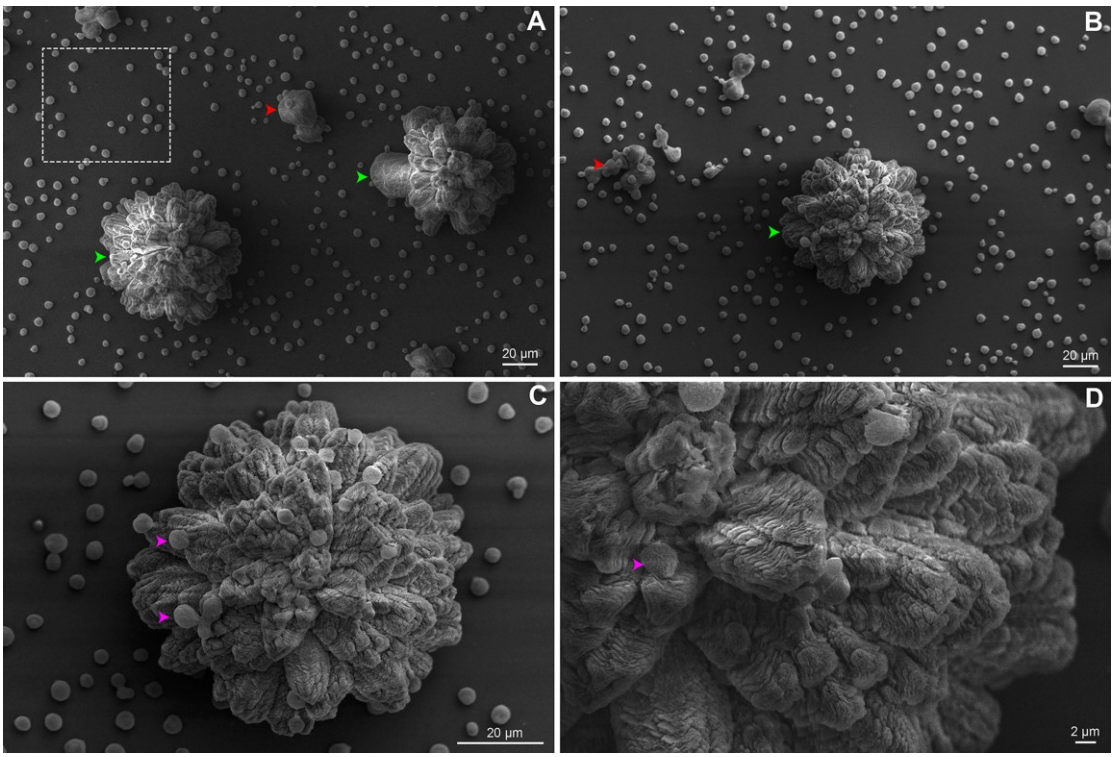

FIG 5 SEM of *C. neoformans* B3501 displaying flower-like clusters. Biofilm presented complex structure and spatial organization. (A) The dotted square indicates cryptococcal cells attached to the surface. (A, B) Biofilm clusters with amorphous and asymmetrical structure (red arrows) and mature biofilm with flower-like shapes (green arrows). Flower-like cluster shown in higher magnification (C, D) with embedded cells in the ECM (pink arrows).

Interestingly, an unexpected phenotype of a few cells located at cluster boundaries, resembling bridges and involved in anchoring the clusters, can be observed. These cells are elongated and interconnect surface substrate and clusters (Fig. 6A-C). We found ECM micro channels displaying a well-designed structure associated with cryptococcal cells (Fig. 6D). For some soil bacteria, the presence of ECM micro channels are required for cell alignment and advancement on surfaces (43).

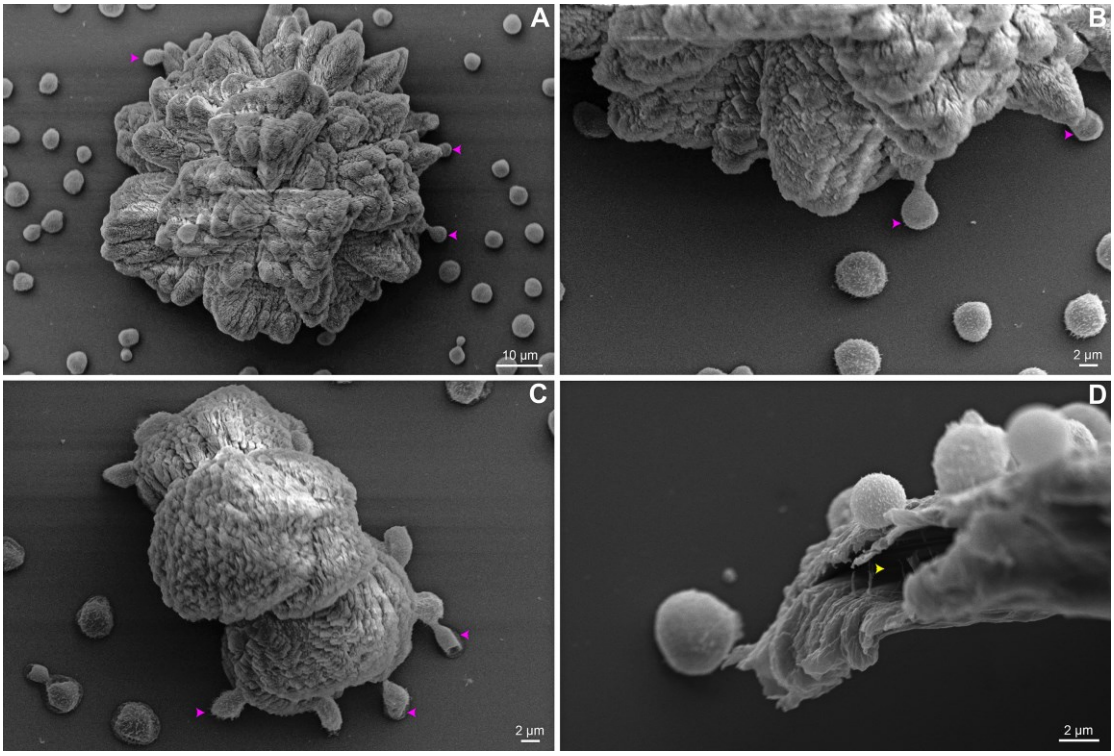

FIG 6 SEM of *C. neoformans* B3501 showing phenotypic cell change and biofilm channel. Anchoring cells (pink arrows) are observed located at the base of some flower-like (A-B) and amorphous (C) clusters boundaries. Micro channels (yellow arrow) are found associated with cells (D).

Cryptococcal biofilms form a social community of clusters.

Even within a community composed of genetically identical microbial cells, there exists high heterogeneity in morphology and physiology of its sub-populations (44). Wang *et al.* (2013), discovered that *C. neoformans* responds in a paracrine manner to a secreted protein responsible for colony communication and morphology (45).

To synchronize social microbial behavior, extracellular signals must disseminate across the community and reach adjacent cells. Here, we speculate the existence of a hierarchical biofilm organization composed of a cluster community. The SEM images show that small clusters (Fig. 7B-D) are adjacent to the mature biofilm cluster (Fig. 7A). We hypothesize that a feedback response of mature clusters signaling leads to the formation of small aggregates surrounded by ECM. The clustering process may implement a secondary signaling for functional or phenotypic switch in a paracrine manner, as supported by Wang. *et al.* (2013). This process seems to trigger an autoinducer activity by stimulating neighboring cells to phenocopy the mature cluster.

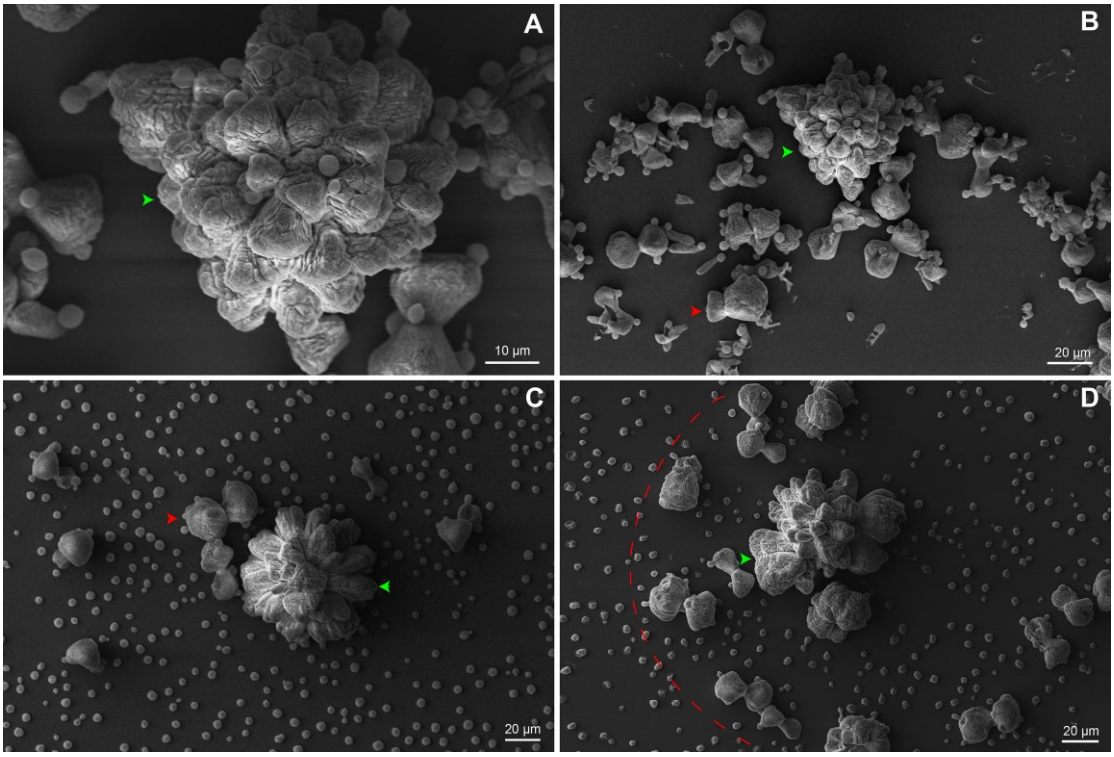

FIG 7 SEM of *C. neoformans* B3501 organized in a community of clusters. (A) Higher magnification image of a mature biofilm. (B-D) Small amorphous clusters (red arrows and dotted arc) surround the mature biofilm (green arrow).

Biofilm associated morphotype switching.

Adhesion is a critical property for biofilm formation. The presence of germ tubes and filamentation in *Candida albicans* enhances and promotes biofilm formation. Thus, suppressing the dimorphic switch is a target for biofilm growth prevention (46, 47). It is well known that *C. neoformans* exhibits yeast, pseudohyphal and hyphal differentiation. A study showed that these morphotypes switches might co-exist in response to adaptation for survival in an unpredictable environmental condition (48) and are driven by multiple communication signals with distinct regulatory patterns (49).

Although the yeast form growth predominates, our finding suggests that pseudohyphae (Fig. 8A) may represent an uncommon but intermediate stage of development related to biofilm formation in segregated populations of *C. neoformans* where ECM is found associated with pseudohyphae (Fig. 8C-D).

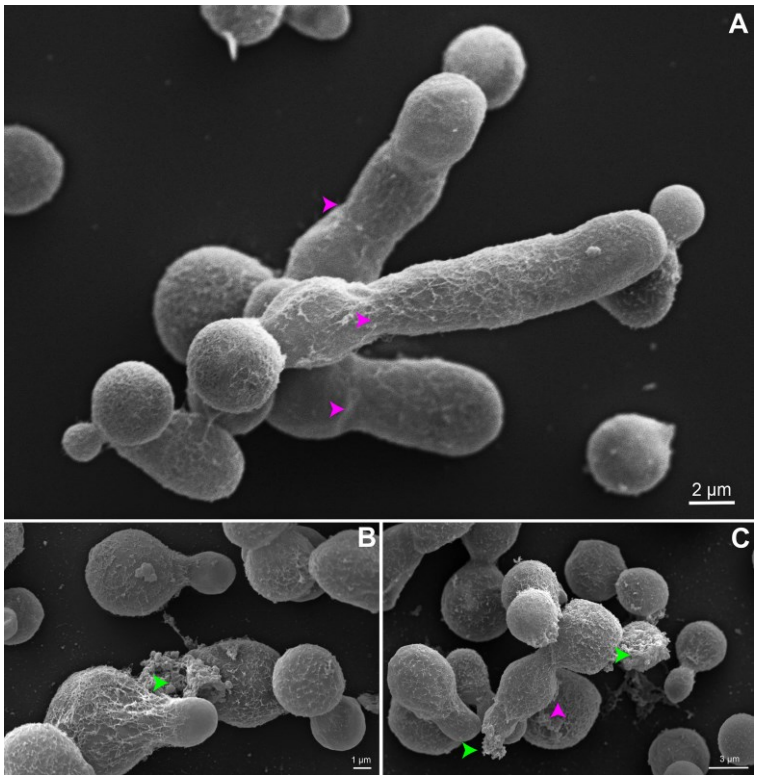

FIG 8 SEM of *C. neoformans* B3501 morphotype switching. (A-C) Different morphotypes can be observed during biofilm formation. Note that the yeast form undergoes a switch to a pseudohyphae phenotype (pink arrow) and are associated with ECM (green arrow).

DISCUSSION

The hallmarks of this study were the use of a numerical measure to quantify the geometrical order of the first layer of adhered cells in the process of biofilm formation as

well as the detection of well-shaped ultrastructure of *C. neoformans* biofilms resembling a flower-like pattern using a novel SEM protocol. To verify the relation between cellular order and biofilm production, we analyzed *C. neoformans* H99 and the mutants *grasp* and *cap67*, and the usual model *C. neoformans* B3501. Once we showed that there is indeed a correlation between increased order and increased biofilm production, we focused on the standard strain to further study the ultrastructure.

This analysis was made possible by the introduction of a modified protocol for SEM visualization of microbial biofilms, due to the fact that standard protocols greatly distort the matrix. To minimize artifacts, a shortened time of fixation and careful dehydration is optimal for ultrastructural SEM analysis (50). The ultrastructure preservation was achieved by combining appropriated techniques, a reduced period of incubation during SEM preparation and good grade reagents.

The predominant structure of biofilms was apparent as an organized dense layer of ECM that functions as a scaffold that permeates the agglomerate, over and among cells. Distinct levels of spatial organization were observed: adhered cells, clusters of cells, as well as the community of clusters. The affinity of attachment to different surfaces is strongly related to the presence of the cryptococcal capsule. In fixed *C. neoformans* cells, the fibers surrounding the cell (capsule filaments) directly stretch and link cells to surface, promoting attachment (19).

Cryptococcal biofilm formation seems to be driven by a communication system via adhesion/matrix protein signaling (45) and directional proliferation of the original adhered cells. Cfl1, the first prominent ECM secreted protein of *C. neoformans*, is highly expressed in subpopulations located at the periphery of a mating community and is concentrated in

the extracellular matrix boundary. This protein orchestrates yeast-hypha morphotype transition, cell adhesion, and virulence. This suggests that Cfl1 may serve as a signal regulating morphotype transition in the cells enclosed or adjacent to the ECM (45, 49, 51).

We hypothesize that the reversible cell attachment is mediated by capsule interactions, including electrostatic repulsion and orderly distribution of cells, as described above. Our data supports that once irreversible attachment occurs, cryptococcal cells may form a narrow ECM layer around the cell body where cells rapidly proliferate, but the surface-attached and peripheral anchored cryptococcal cells may restrict their expansion to the plane. As initial small clusters proliferate, their shape increasingly becomes anisotropic. At this point, the biofilm consists of several layers of cells grouped into clusters resembling extremely organized flower-like patterns. After maturation, cells may detach as microcolonies or as isolated planktonic cells, which auto-organize following an approximately hexagonal distribution. Cells tend to follow similar trajectories and may initiate the process again (Fig. 9 and Movie S1).

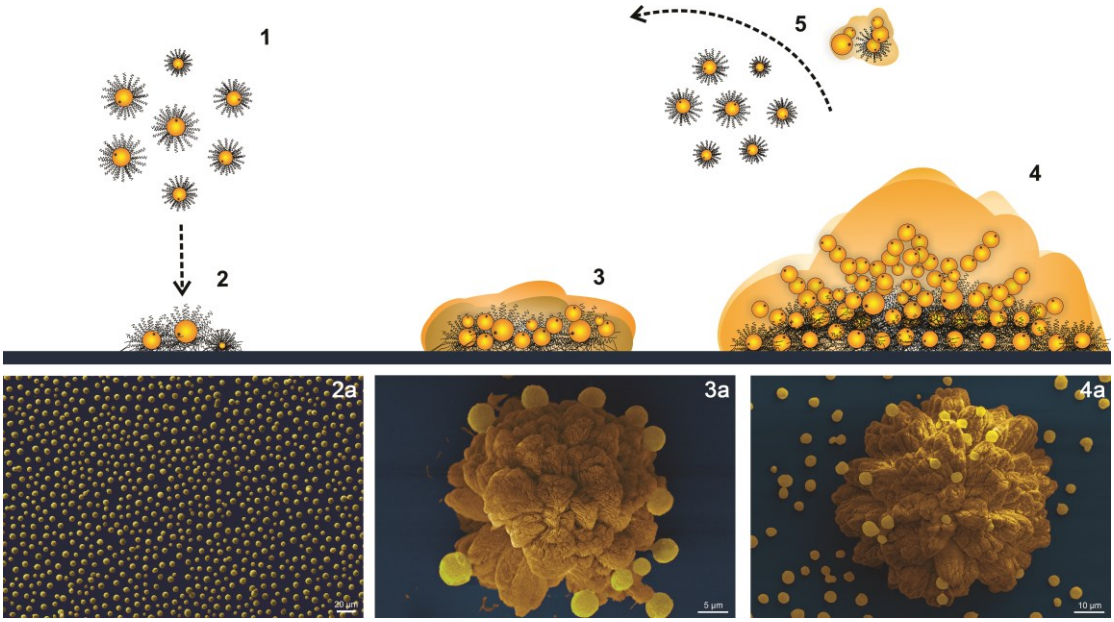

FIG 9 Scheme of *C. neoformans* B3501 biofilm formation. (1-2) Adhesion of planktonic cells follows an approximately hexagonal distribution. (3) Cluster expansion and shaping. (4) Flower-like mature biofilm. (5) Detachment of microcolonies or planktonic cells. (a) SEM of biofilm development stages.

Yan *et al.* (2016) discovered that the cluster ultrastructure of *Vibrio cholerae* biofilm results from the combination of expansion and confinement of surface-attached cells that generates an effective anisotropic stress. Such stress overpowers the cell-to-surface adhesion force for cells at the cluster center, causing these cells to realign in the vertical direction and forcing the transition from 2D expansion to 3D growth (52). Moreover, if selection pressure is high, it has been shown that clusters of *Pseudomonas aeruginosa* have higher fitness than isolated cells because cells at the top of the clusters have better access to nutrients (53). Cluster morphogenesis results from a great number of variables capable of shaping the ultrastructure. Physical and demographic processes are demonstrated to act as key factors in biofilm architectures (54). Cryptococcal cells are

likely most susceptible to the hydrodynamics constraints due to low motility. In contrast, more motile microorganisms may escape these constraints and develop biofilm morphogenesis related to cellular migration and biofilm coalescence (54).

Mathematical studies have related that biofilm architecture depends on the availability of nutrients, carbon and oxygen, uptake processes linked to hydrodynamics and diffusion limitation of substrate transport through the biofilm. More generally, metabolic capabilities, genotypic and phenotypic adaptations could result in different behaviors within the biofilm, allowing organisms to choose between a number of strategies (55, 56).

Interestingly, for *V. cholerae* the presence of low cell number in cluster biofilm results in increased volume when compared to biofilms with a larger population. The hypothesis is that the significant changes in cell–cell spacing between small and large clusters in biofilms are due to strong temporal variation in ECM composition or production levels per cell (7). In agreement, the flower-like cluster of *C. neoformans* presents a high volume of ECM and relatively low cell concentration.

From a clinical point of view, understanding biofilm formation and morphology may help develop methods to inhibit the colonization of medical devices. For instance, the shunting procedures used to treat cryptococcal meningitis hypertension are risk associated and have historically discouraged surgeons due to its complications (57, 58) since it can provide a surface for cryptococcal attachment. It is common knowledge that uropathogenic strains of *Escherichia coli* can successfully adhere to and colonize the kidney, despite the presence of high flow rates. Since kidney tubules are narrow (<50

μm), bacterial attachment patterns at even very small spatial scales can easily block them, increasing the severity of kidney infection (59).

Upon this scenario, special treatment of the devices or the use of materials that hinder the initial organization may be used clinically to avoid the development of infection, by disrupting the initial organization. Moreover, the introduction of an objective measure of order (ψ_6) obtained from an image may facilitate the analysis of whether a given surface is prone to biofilm formation. Continued studies are required to provide a greater understanding of the importance to investigate the complications of cryptococcal meningoencephalitis associated to the spatial distribution of clusters, as well as new methods of imaging for helping the development of new anti-biofilm targets.

MATERIALS & METHODS

Quantification of *Cryptococcus neoformans* biofilm formation by XTT.

C. neoformans var. *neoformans* strain B3501, *C. neoformans* var. *grubii* strain H99 and mutants *cap67* (40) and *grasp* (39) were grown for 24 h at 30 °C, in 25 mL of *Sabouraud* broth media in a rotary shaker at 150 rpm. Cells were then collected by centrifugation at 3,000 *g* for 5 min, washed three times with phosphate-buffered saline pH 7.2 (PBS), counted using a hemacytometer and suspended at 10^7 cells/mL in DMEM - Dubelcco's modified eagle media high glucose (GIBCO, USA) at pH 7.4. After that, 500 μL of the suspension were added into individual wells of polystyrene 24-well plates (Greiner Bio-One, AUS) containing sterile glass coverslips and incubated at 37 °C for 48 h. Following incubation, wells were washed in triplicate with PBS to remove any

planktonic cells. Then, 300 µL of XTT salt solution (1 mg/ml in PBS) and 24 µL of menadione solution (1 mM in acetone; Sigma-Aldrich) were added to each well. Microtiter plates were incubated at 37 °C for 5 h. Mitochondrial dehydrogenases in live cells reduce XTT tetrazolium salt to XTT formazan, resulting in a colorimetric change, which was measured in a microtiter reader at 492 nm (SpectraMax i3). Microtiter wells containing only culture media but no *C. neoformans* cells were used as negative controls. Prior studies demonstrated that the XTT reduction assay measurements correlate with biofilm and fungal cell number (29).

Geometric analysis.

The strains were allowed to grow for 4h (adhesion stage) in the conditions above described. Following the incubation, the wells were washed three times and prepared for SEM. Images were treated with the software ImageJ (version1.48k, Java 1.8.0_65 (64-bit); National Institutes of Health, USA, [http://imagej.nih.gov/ij]) to extract information for further statistical analysis. An ellipse was fitted to each of the particles in the image and its area was calculated. Since only the center coordinates of each ellipse are necessary for the analysis of the neighboring cells network, we represent particles with circles of fixed radius such that their areas are equal to the average ellipse area. Once the centers are defined, it is possible to establish the nearest neighbors of each cell n_i by means of a Delaunay triangulation and Voronoi tessellation using Fortune's algorithm (60) with the software voronoi (version 1, Steve J. Fortune, Bell Laboratories, USA [http://ect.bell-labs.com/who/sjf/voronoi.tar]) With this information, it is possible to obtain the number of

nearest neighbors and distance distributions, allowing one to calculate average parameters that quantify order in the spatial distribution of cells for each sample image.

To calculate the local variance in the number of neighbors μ_2^i, first the average number of neighbors was calculated for the sample

$$n = \langle n_i \rangle = \frac{1}{N}\sum_{i=1}^{\mathrm{N}} n_i, \quad (1)$$

where N is the number of cells whose distance to any image border is not within 5 % of the system size. Cells close to the border were not taken into account to calculate bulk properties. The local variance was defined as

$$\mu_2^i = (\mathrm{n_i} - n)^2, \quad (2)$$

and the global variance was defined as its average

$$\mu_2 = \langle \mu_2^i \rangle = \frac{1}{N}\sum_{i=1}^{\mathrm{N}} \mu_2^i. \quad (3)$$

Following Borba *et al.* (38) we calculate the local order parameter

$$\psi_6^i = \frac{1}{n_i}\sum_{j=1}^{\mathrm{n_i}} cos\left(6\theta_{ijk}\right), \quad (4)$$

where θ_{ijk} are the angles formed by the two line segments joining site j and two of its consecutive neighbors (Fig. 10).

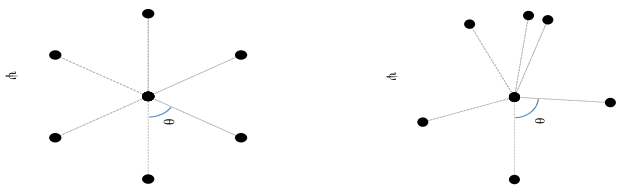

FIG 10 Values of ψ_6^i for a site in a triangular lattice (left) and for a random distribution of neighbors (right).

A given set of points (an image) can then be characterized by the average value of this quantity

$$\psi_6 = \langle \psi_6^i \rangle = \frac{1}{N} \sum_{i=1}^{N} \psi_6^i. \qquad (5)$$

For a triangular lattice of points, every site will have $\psi_6^i = 1$, since every site has six neighbors and six angles equal to $60\,°$. Therefore, $\psi_6 = 1$, characterizes a perfect hexagonal symmetry (38). On the other hand, for a set of randomly distributed points, a value of $\psi_6$close to 0 is expected.

In order to analyze the probability of generating a given value of ψ_6 from a random distribution of points, we generated 1000 sets of randomly distributed non-overlapping disks with areas equal to the average area of a cell in a box of the same size as that of the image. For such an ensemble with N_e images (sets of points), one can calculate the average $\langle \psi_6 \rangle$ of $\psi_6$and its standard deviation. Then, it is possible to apply a Student-t test to evaluate the possibility that the values of ψ_6 for experimental configurations of cells

present the same distribution as those for a random configuration generated by the deposition of non-overlapping disks. The one-tailed test for samples with unequal variance was calculated using LibreOffice (version 4.2.8.2 Build ID: 420m0 (Build: 2); LibreOffice, The Document Foundation, [http://www.libreoffice.org]). The p-values of the test were obtained for the 3 pairs of data: a) 5 samples of B3501 with 1000 sets of non-overlapping disks ($p \approx 3.7 \times 10^{-7}$); b) 5 samples of H99 with 1000 sets of non-overlapping disks ($p \approx 0.35$); c) 5 samples of B3501 with 5 samples of H99 ($p \approx 1.1 \times 10^{-6}$). In Fig. S2 we show the corresponding network for a set of randomly distributed non-overlapping disks and the distribution of ψ_6 for 1000 random sets.

Scanning electron microscopy preparation.

An improved protocol developed for visualization of *C. neoformans* planktonic cells by electron microscopy was recently described (20). Here, we modified a few parameters in order to preserve the ultrastructure of the biofilm stages. Briefly, after the incubation period (4 h for adhesion or 48 h for mature biofilm) as previously described the wells containing the coverslips were washed three times with PBS. After washing, cryptococcal adhered cells were fixed with 500 µL of 2.5 % glutaraldehyde type 1 (Sigma Aldrich, USA) diluted in 0.1 M sodium cacodylate buffer pH 7.2 and for 15 minutes at room temperature. Then, the wells were washed three times in 0.1 M sodium cacodylate buffer pH 7.2 containing 0.2 M sucrose and 2 mM $MgCl_2$ with the aid of two pipettors, which were used for addition and concurrent removal to avoid air exposure. Adhered cells were dehydrated in a series of freshly made solutions of graded ethanol (30, 50 and 70%, for 5 min/step, then 95% and twice 100%, for 10 min/step). The dehydration was closely monitored to

prevent biofilm matrix and capsule polysaccharide extraction. Samples were then subjected to critical point drying (EM CPD 300, Leica) immediately after dehydration, mounted on metallic stubs, sputter-coated with a 15–20 nm gold-palladium layer and visualized in a scanning electron microscope (Carl Zeiss EVO® MA10 or EVO® -50HV Carl, Oberkochen, Germany), operating at 10kV. Microscopic fields were selected by random scanning and photo documented. The experiment was performed in three independent replicates.

Time-lapse microscopy.

C. nerformans B3501 cells were prepared as described above and suspended at 10^6 cells/mL in DMEM. After that, 1 mL of the suspension was added into individual wells of glass and incubated for 4 h at 37 °C. Following incubation, wells were washed in triplicate with PBS to remove planktonic cells. Then, 1 mL of DMEM was replaced and the wells incubated for 48 h at 37 °C on an Espectral FV 1000 system. Time-lapses were performed for at 30–60-s intervals.

SUPLEMENTAL MATERIALS

Fig. S1: Values of the local variance of the number of nearest neighbors μ_2^i.

Fig. S2: Set of randomly distributed non-overlapping disks and distribution of ψ_6 for 1000 random sets.

Movie S1: Time-lapse microscopy of *C. neoformans* B3501 flow during biofilm various stages of biofilm.

Table S1: Geometrical properties of 5 biological replicates of *C. neoformans* B3501 and H99, for conditions with and without poly-L-lysine.

ACKNOWLEDGEMENTS

This work was supported by Conselho Nacional de Desenvolvimento Científico e Tecnológico(CNPq). We thank Dr. Kildare Miranda and Rachel Rachid from CENABIO-UFRJ for their support. We thank Dr. Marcio L. Rodrigues from FIOCRUZ/UFRJ for carefully reading the manuscript and for valuable comments.

FUNDING INFORMATION

This work was supported by grants from the Brazilian agencies Conselho Nacional de Desenvolvimento Científico e Tecnológico (CNPq) and Coordenação de Aperfeiçoamento de Pessoal de Nível Superior (CAPES). The funding agencies had no participation on the decision of the study subject, data collection and analysis or on the submission of this work for publication.

REFERENCES

1. Jabra-Rizk MA, Falkler WA, Meiller TF. 2004. Fungal biofilms and drug resistance. Emerg Infect Dis 10:14-9.

2. Costerton JW, Lewandowski Z, Caldwell DE, Korber DR, Lappin-Scott HM. 1995. Microbial biofilms. Annu Rev Microbiol 49:711-45.
3. Ramage G, Mowat E, Jones B, Williams C, Lopez-Ribot J. 2009. Our current understanding of fungal biofilms. Crit Rev Microbiol 35:340-55.
4. Martinez LR, Casadevall A. 2015. Biofilm Formation by Cryptococcus neoformans. Microbiol Spectr 3.
5. Watnick P, Kolter R. 2000. Biofilm, city of microbes. J Bacteriol 182:2675-9.
6. Parsek MR, Fuqua C. 2004. Biofilms 2003: emerging themes and challenges in studies of surface-associated microbial life. J Bacteriol 186:4427-40.
7. Drescher K, Dunkel J, Nadell CD, van Teeffelen S, Grnja I, Wingreen NS, Stone HA, Bassler BL. 2016. Architectural transitions in Vibrio cholerae biofilms at single-cell resolution. Proc Natl Acad Sci U S A doi:10.1073/pnas.1601702113.
8. Sheppard DC, Howell PL. 2016. Biofilm Exopolysaccharides of Pathogenic Fungi: Lessons from Bacteria. J Biol Chem doi:10.1074/jbc.R116.720995.
9. Gulati M, Nobile CJ. 2016. Candida albicans biofilms: development, regulation, and molecular mechanisms. Microbes Infect doi:10.1016/j.micinf.2016.01.002.
10. Stacy A, McNally L, Darch SE, Brown SP, Whiteley M. 2016. The biogeography of polymicrobial infection. Nat Rev Microbiol 14:93-105.
11. Flemming HC, Wingender J. 2010. The biofilm matrix. Nat Rev Microbiol 8:623-33.
12. Chandra J, Kuhn DM, Mukherjee PK, Hoyer LL, McCormick T, Ghannoum MA. 2001. Biofilm formation by the fungal pathogen Candida albicans: development, architecture, and drug resistance. J Bacteriol 183:5385-94.

13. Mundy RD, Cormack B. 2009. Expression of Candida glabrata adhesins after exposure to chemical preservatives. J Infect Dis 199:1891-8.
14. Donlan RM. 2002. Biofilms: microbial life on surfaces. Emerg Infect Dis 8:881-90.
15. Martinez LR, Casadevall A. 2006. Cryptococcus neoformans cells in biofilms are less susceptible than planktonic cells to antimicrobial molecules produced by the innate immune system. Infect Immun 74:6118-23.
16. Lewis K. 2008. Multidrug tolerance of biofilms and persister cells. Curr Top Microbiol Immunol 322:107-31.
17. Clatworthy AE, Pierson E, Hung DT. 2007. Targeting virulence: a new paradigm for antimicrobial therapy. Nat Chem Biol 3:541-8.
18. Rajasingham R, Smith RM, Park BJ, Jarvis JN, Govender NP, Chiller TM, Denning DW, Loyse A, Boulware DR. 2017. Global burden of disease of HIV-associated cryptococcal meningitis: an updated analysis. Lancet Infect Dis doi:10.1016/S1473-3099(17)30243-8.
19. de S Araújo GR, Fontes GN, Leão D, Rocha GM, Pontes B, Sant'Anna C, de Souza W, Frases S. 2016. Cryptococcus neoformans capsular polysaccharides form branched and complex filamentous networks viewed by high-resolution microscopy. J Struct Biol 193:75-82.
20. Martinez LR, Mihu MR, Han G, Frases S, Cordero RJ, Casadevall A, Friedman AJ, Friedman JM, Nosanchuk JD. 2010. The use of chitosan to damage Cryptococcus neoformans biofilms. Biomaterials 31:669-79.
21. Rodrigues ML, Nimrichter L, Oliveira DL, Frases S, Miranda K, Zaragoza O, Alvarez M, Nakouzi A, Feldmesser M, Casadevall A. 2007. Vesicular

polysaccharide export in Cryptococcus neoformans is a eukaryotic solution to the problem of fungal trans-cell wall transport. Eukaryot Cell 6:48-59.

22. Park BJ, Wannemuehler KA, Marston BJ, Govender N, Pappas PG, Chiller TM. 2009. Estimation of the current global burden of cryptococcal meningitis among persons living with HIV/AIDS. AIDS 23:525-30.

23. Martinez LR, Casadevall A. 2005. Specific antibody can prevent fungal biofilm formation and this effect correlates with protective efficacy. Infect Immun 73:6350-62.

24. Banerjee U, Gupta K, Venugopal P. 1997. A case of prosthetic valve endocarditis caused by Cryptococcus neoformans var. neoformans. J Med Vet Mycol 35:139-41.

25. Braun DK, Janssen DA, Marcus JR, Kauffman CA. 1994. Cryptococcal infection of a prosthetic dialysis fistula. Am J Kidney Dis 24:864-7.

26. Shah NB, Shoham S, Nayak S. 2015. Cryptococcus neoformans prosthetic joint infection: case report and review of the literature. Mycopathologia 179:275-8.

27. Johannsson B, Callaghan JJ. 2009. Prosthetic hip infection due to Cryptococcus neoformans: case report. Diagn Microbiol Infect Dis 64:76-9.

28. Walsh TJ, Schlegel R, Moody MM, Costerton JW, Salcman M. 1986. Ventriculoatrial shunt infection due to Cryptococcus neoformans: an ultrastructural and quantitative microbiological study. Neurosurgery 18:373-5.

29. Aslanyan L, Sanchez D, Valdebenito S, Eugenin E, Ramos R, Martinez L. 2017. The Crucial Role of Biofilms in Cryptococcus neoformans Survival within

Macrophages and Colonization of the Central Nervous System. Journal of Fungi 3:10.

30. Martinez LR, Casadevall A. 2007. Cryptococcus neoformans biofilm formation depends on surface support and carbon source and reduces fungal cell susceptibility to heat, cold, and UV light. Appl Environ Microbiol 73:4592-601.

31. Edwards MR, Gordon MA, Lapa EW, Ghiorse WC. 1967. Micromorphology of Cryptococcus neoformans. J Bacteriol 94:766-77.

32. Sakaguchi N. 1993. Ultrastructural study of hepatic granulomas induced by Cryptococcus neoformans by quick-freezing and deep-etching method. Virchows Arch B Cell Pathol Incl Mol Pathol 64:57-66.

33. Nelson D. 2002. Defects and Geometry in Condensed Matter Physics. *Cambridge University Press*.

34. Bernard EP, Krauth W. 2011. Two-step melting in two dimensions: first-order liquid-hexatic transition. Phys Rev Lett 107:155704.

35. Nelson DR, Halperin BI. 1979. Dislocation-mediated melting in two dimensions. Physical Review B 19:2457-2484.

36. Aeppli G, Bruinsma R. 1984. Hexatic Order and Liquid Density Fluctuations. Physical Review Letters 53:2133-2136.

37. Okabe A, Boots B, Sugihara K, Chiu SN, Kendall DG. 2008. Definitions and Basic Properties of Voronoi Diagrams, p 43-112, Spatial Tessellations doi:10.1002/9780470317013.ch2. John Wiley & Sons, Inc.

38. Borba JR, Brito C, Migowski P, Vale TB, Stariolo DA, Teixeira SR, Feil AF. 2013. Quantitative Characterization of Hexagonal Packings in Nanoporous Alumina Arrays: A Case Study. The Journal of Physical Chemistry C 117:246-251.
39. Kmetzsch L, Joffe LS, Staats CC, de Oliveira DL, Fonseca FL, Cordero RJ, Casadevall A, Nimrichter L, Schrank A, Vainstein MH, Rodrigues ML. 2011. Role for Golgi reassembly and stacking protein (GRASP) in polysaccharide secretion and fungal virulence. Mol Microbiol 81:206-18.
40. Fromtling RA, Shadomy HJ, Jacobson ES. 1982. Decreased virulence in stable, acapsular mutants of cryptococcus neoformans. Mycopathologia 79:23-9.
41. Robertson EJ, Casadevall A. 2009. Antibody-mediated immobilization of Cryptococcus neoformans promotes biofilm formation. Appl Environ Microbiol 75:2528-33.
42. Martinez LR, Casadevall A. 2006. Susceptibility of Cryptococcus neoformans biofilms to antifungal agents in vitro. Antimicrob Agents Chemother 50:1021-33.
43. Berleman JE, Zemla M, Remis JP, Liu H, Davis AE, Worth AN, West Z, Zhang A, Park H, Bosneaga E, van Leer B, Tsai W, Zusman DR, Auer M. 2016. Exopolysaccharide microchannels direct bacterial motility and organize multicellular behavior. ISME J 10:2620-2632.
44. Lidstrom ME, Konopka MC. 2010. The role of physiological heterogeneity in microbial population behavior. Nat Chem Biol 6:705-12.
45. Wang L, Tian X, Gyawali R, Lin X. 2013. Fungal adhesion protein guides community behaviors and autoinduction in a paracrine manner. Proc Natl Acad Sci U S A 110:11571-6.

46. Zhang Y, Cai C, Yang Y, Weng L, Wang L. 2011. Blocking of Candida albicans biofilm formation by cis-2-dodecenoic acid and trans-2-dodecenoic acid. J Med Microbiol 60:1643-50.

47. You J, Du L, King JB, Hall BE, Cichewicz RH. 2013. Small-molecule suppressors of Candida albicans biofilm formation synergistically enhance the antifungal activity of amphotericin B against clinical Candida isolates. ACS Chem Biol 8:840-8.

48. Lee SC, Phadke S, Sun S, Heitman J. 2012. Pseudohyphal growth of Cryptococcus neoformans is a reversible dimorphic transition in response to ammonium that requires Amt1 and Amt2 ammonium permeases. Eukaryot Cell 11:1391-8.

49. Wang L, Lin X. 2015. The morphotype heterogeneity in Cryptococcus neoformans. Curr Opin Microbiol 26:60-4.

50. Joubert L-M, Ferreira J, Stevens D. 2015. Aspergillus fumigatus Biofilms: a Comparison of Processing Techniques for Scanning Electron Microscopy of Fungal Mycelium and Extracellular Matrix., vol 21, p 935-936.

51. Wang L, Zhai B, Lin X. 2012. The link between morphotype transition and virulence in Cryptococcus neoformans. PLoS Pathog 8:e1002765.

52. Yan J, Sharo AG, Stone HA, Wingreen NS, Bassler BL. 2016. Vibrio cholerae biofilm growth program and architecture revealed by single-cell live imaging. Proc Natl Acad Sci U S A 113:E5337-43.

53. Kragh KN, Hutchison JB, Melaugh G, Rodesney C, Roberts AE, Irie Y, Jensen P, Diggle SP, Allen RJ, Gordon V, Bjarnsholt T. 2016. Role of Multicellular Aggregates in Biofilm Formation. MBio 7:e00237.

54. Hödl I, Mari L, Bertuzzo E, Suweis S, Besemer K, Rinaldo A, Battin TJ. 2014. Biophysical controls on cluster dynamics and architectural differentiation of microbial biofilms in contrasting flow environments. Environ Microbiol 16:802-12.

55. Klapper I, Szomolay B. 2011. An exclusion principle and the importance of mobility for a class of biofilm models. Bull Math Biol 73:2213-30.

56. Klapper I. 2012. Productivity and equilibrium in simple biofilm models. Bull Math Biol 74:2917-34.

57. Cherian J, Atmar RL, Gopinath SP. 2016. Shunting in cryptococcal meningitis. J Neurosurg 125:177-86.

58. Liu L, Zhang R, Tang Y, Lu H. 2014. The use of ventriculoperitoneal shunts for uncontrollable intracranial hypertension in patients with HIV-associated cryptococcal meningitis with or without hydrocephalus. Biosci Trends 8:327-32.

59. Melican K, Sandoval RM, Kader A, Josefsson L, Tanner GA, Molitoris BA, Richter-Dahlfors A. 2011. Uropathogenic Escherichia coli P and Type 1 fimbriae act in synergy in a living host to facilitate renal colonization leading to nephron obstruction. PLoS Pathog 7:e1001298.

60. Fortune S. 1987. A sweepline algorithm for Voronoi diagrams. Algorithmica 2:153.

SUPPLEMENTAL MATERIAL – FIGURE S1

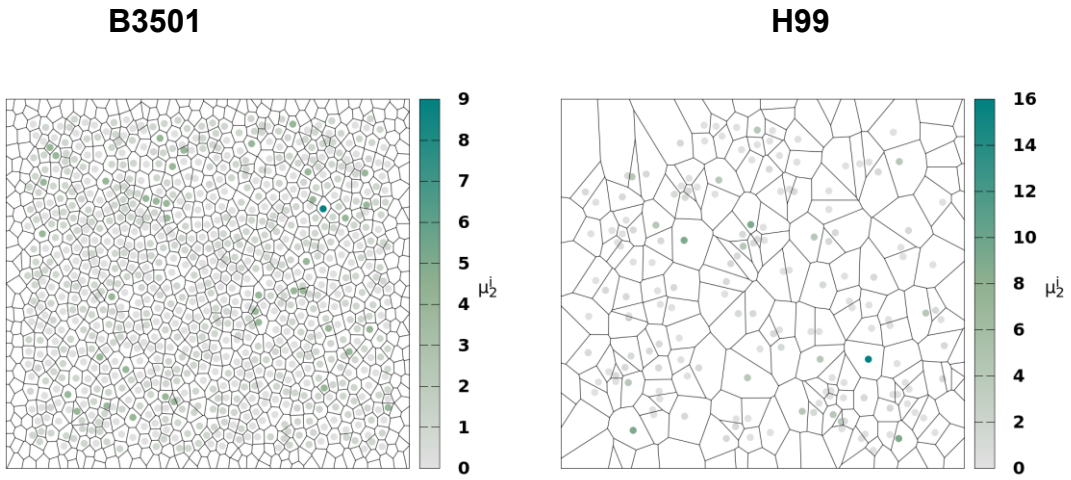

FIG S1 Analysis of the variance of the number of nearest neighbors, μ_2^i, for samples without Poly-L-lysine. Left: *C. neoformans* B3501. Right: *C. neoformans* H99.

SUPPLEMENTAL MATERIAL – FIGURE S2

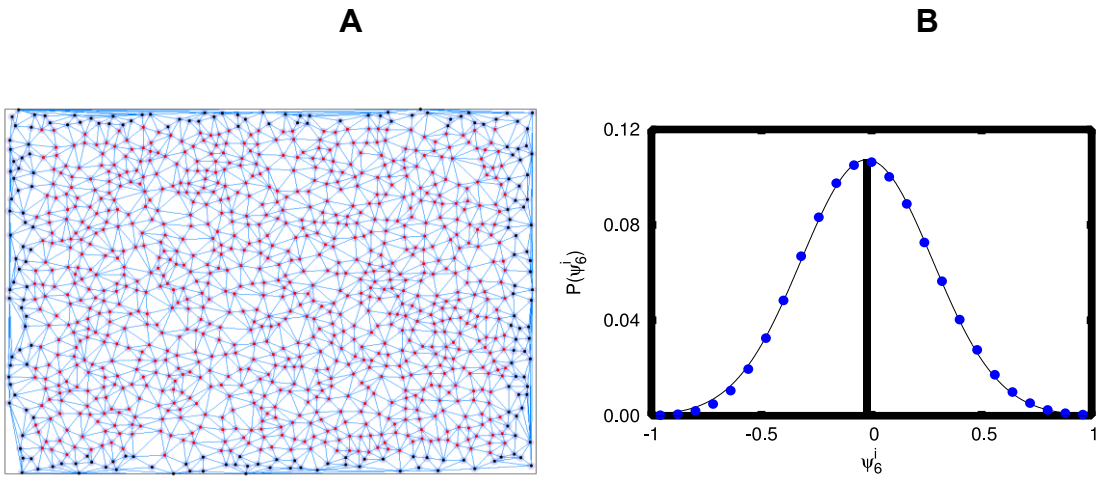

FIG S2 A) Blue line segments compose the Delaunay triangulation network for a randomly distributed set of disks, which are not allowed to overlap (the minimum distance between 2 disks is $2R$, where the disk radius is $R \approx 7.6$ pixels, corresponding to the average cell radius of Fig. 2A). To minimize border effects, disks lying close to a boundary (a distance within 5% of the figure length) were discarded (black dots) for the calculation of ψ_6 ($\psi_6 \approx 0.0096$, N = 867, N_{tot} = 1064). B) Distribution of ψ_6 for 1000 independent samples with the same parameters: the vertical line corresponds to the average $\langle\psi_6\rangle \approx -0.013816$. The dimensions of the box are $L_x = 1024$ and $L_y = 768$ pixels, equal to those of the image in Fig 2A.

Sheet1

Geometrical properties of 5 biological replicates

***C. neoformans* H99 Biofilm with Poly-L-lysine (P+)**

sample	ψ6	μ2	n	r	N_tot	N_analized
2	0.048	1.09	6.005	31.8	944	740
3	0.028	1.52	5.988	24.0	1495	1210
4	0.052	1.01	6.005	33.7	818	642
5	0.065	1.00	6.007	32.8	885	699
6	0.048	0.97	6.006	33.6	843	646
AVE	**0.048**	**1.12**	**6.002**	**31.2**	**997**	**787**
AVE_STD	**0.006**	**0.10**	**0.004**	**1.8**	**126**	**107**

***C. neoformans* H99 Biofilm without Poly-L-lysine (P-)**

sample	ψ6	μ2	n	r	N_tot	N_analized
1	-0.066	1.74	5.898	66.2	247	196
2	-0.029	1.62	5.922	73.4	213	166
3	-0.058	1.64	5.889	72.6	209	171
4	-0.039	2.09	5.871	80.4	179	140
5	0.006	2.01	5.930	60.5	272	215
AVE	**-0.037**	**1.82**	**5.902**	**70.6**	**224**	**178**
AVE_STD	**0.013**	**0.10**	**0.011**	**3.4**	**16**	**13**

***C. neoformans* B3501 Biofilm with Polylysine-L-lysine (P+)**

sample	ψ6	μ2	n	r	N_tot	N_analized
2	0.231	0.748	5.997	28.41	1103	873
3	0.217	0.828	6.007	29.20	1064	836
4	0.239	0.702	6.001	29.36	1032	810
5	0.221	0.768	6.001	29.01	1066	837
6	0.202	0.755	6.009	29.20	1056	822
AVE	**0.222**	**0.760**	**6.003**	**29.04**	**1064**	**836**
AVE_STD	**0.006**	**0.020**	**0.002**	**0.17**	**11**	**11**

***C. neoformans* B3501 Biofilm without Polylysine-L-lysine (P-)**

sample	ψ6	μ2	n	r	N_tot	N_analized
1	0.213	0.667	6.0000	30.76	1064	842
2	0.200	0.774	5.9945	29.67	1151	913
3	0.200	0.716	5.9978	29.97	1127	894
4	0.185	0.723	5.9988	30.53	1088	856
6	0.199	0.687	6.0093	30.40	1099	862
AVE	**0.199**	**0.714**	**6.0001**	**30.27**	**1106**	**873**
AVE_STD	**0.004**	**0.018**	**0.0025**	**0.20**	**15**	**13**

n: average number of neighbors; r: average distance between cells; N: number of cells in the image; AVE: averages; AVE_STD: standard deviations of the means

Average values over 5 biological replicates

	<ψ6>	std_<ψ6>	<μ2>	std_<μ2>	<n>	std_<n>	<r>	std_<r>	<XTT>	std_<XTT>
P+ H99	**0.048**	**0.006**	**1.12**	**0.10**	**6.002**	**0.004**	**31.2**	**1.8**	**0.890**	**0.022**
P+ B350	**0.222**	**0.006**	**0.760**	**0.020**	**6.003**	**0.002**	**29.04**	**0.17**	**1.57**	**0.05**
P- H99	**-0.037**	**0.012**	**1.82**	**0.10**	**5.902**	**0.011**	**70.6**	**3.4**	**0.44**	**0.03**
P- B3501	**0.199**	**0.004**	**0.714**	**0.018**	**6**	**0.0025**	**30.27**	**0.2**	**1.380**	**0.010**